Further Insight into Interfacial Interactions in Iron/Liquid Zn-Al System

DAVID ZAPICO-ÁLVAREZ, PATRICK BARGES, CÉLINE MUSIK, FLORENCE BERTRAND, JEAN-MICHEL MATAIGNE, MARION DESCOINS, DOMINIQUE MANGELINCK, and MARIE-LAURENCE GIORGI

In the galvannealing process, steel strips are immersed in molten zinc containing 0.100 to 0.135 wt pct Al at 450 °C. The coating obtained is composed of a thin intermetallic compounds' layer called the inhibition layer (200 nm) covered with a thick zinc layer (10 μm). The nature of this inhibition layer has been investigated here for a galvanizing bath with a low Al content. The inhibition layer formed on industrial low-alloyed steels was characterized by transmission electron microscopy and atom probe tomography. The inhibition layer is composed of a thin $Fe_2Al_5Zn_x$ layer (20 nm), covered with a thicker δ layer (200 nm). The $Fe_2Al_5Zn_x$ layer is discontinuous at the lowest bath Al content. Small precipitates (20 nm in diameter) with a stoichiometry corresponding to Fe_3Al-containing Zn were also found for the first time in the δ phase. The microstructure of the inhibition layer can be described with diffusion paths drawn in the Al-Fe-Zn ternary section at 450 °C. This means that all interfaces of the inhibition layer are at thermodynamic equilibrium. The $Fe_2Al_5Zn_x$ layer is formed on the steel surface before the δ layer. The nucleation and growth of the Fe_3Al-Zn particles probably occur in the liquid metal at the same time as δ.

I. INTRODUCTION

STEEL strip is often coated with a layer of zinc in order to protect it against corrosion. One of the most commonly used coating processes is continuous hot-dip galvanizing. In this process, the steel strip is immersed in a molten zinc bath containing small amounts of aluminum at about 450 °C. Aluminum is added to the liquid zinc bath in order to cause the growth of a very thin Al-containing alloy layer, generally called *inhibition layer*, as it prevents, although temporarily, the uncontrolled growth of solid Fe-Zn intermetallic compounds. When the strip exits the bath, the thickness of the dragged molten metal film is too high and set at its final value by gas wiping. The coated sheet is then either cooled by forced air (GalvanIzed or GI products) or subjected to an in-line heat treatment called galvannealing (GalvAnnealed or GA products). The objective of this additional step is to activate very well-controlled Fe-Zn alloying reactions in order to obtain a final coating fully composed of a sequence of Fe-Zn intermetallic compounds.[1] To enhance the kinetics of these reactions, the Al content in GA baths (around 0.1 wt pct) is lowered compared to the one in GI baths (around 0.2 wt pct).

The study presented here will focus on the reactions that occur in GA bath, *i.e.*, Fe-saturated Zn bath with Al content ranging from 0.10 to 0.135 wt pct.

In GA baths, the inhibition layer acts as a transient barrier that is destabilized during the galvannealing heat treatment when Fe and Zn interdiffusion is accelerated by higher temperatures. This phenomenon, commonly known as inhibition rupture, represents a key point in the GA process.[1,2]

From an industrial point of view, a precise knowledge of the structure and composition of the inhibition layer is crucial to ensure or improve the quality of GA coatings for at least two reasons. First of all, as the kinetics for the inhibition rupture is controlled by diffusion mechanisms in the inhibition layer, its nature is expected to play a direct role on the quality of the final coating: a discontinuous or heterogeneous inhibition layer, either in thickness or in composition, may conduct

DAVID ZAPICO-ÁLVAREZ is with the ArcelorMittal Global R&D - Maiziéres Automotive Products, Voie Romaine BP 30320, 57283 Maiziéres-lés-Metz, France and also with the CentraleSupélec, Université Paris Saclay, 3 rue Joliot-Curie, 91 192 Gif-sur-Yvette Cedex, France. PATRICK BARGES, CÉLINE MUSIK, FLORENCE BERTRAND, and JEAN-MICHEL MATAIGNE are with the ArcelorMittal Global R&D - Maiziéres Automotive Products. MARION DESCOINS and DOMINIQUE MANGELINCK are with the IM2NP, UMR CNRS 7334, Université d'Aix-Marseille et de Toulon, Faculté des Sciences Saint Jérôme, Avenue Escadrille Normandie Niemen, 13 397 Marseille Cedex, France. MARIE-LAURENCE GIORGI is with the CentraleSupélec, Université Paris Saclay. Contact e-mail: marie-laurence.giorgi@centralesupelec.fr

to a heterogeneous final coating. Secondly, the production of high-quality GA coatings demands an accurate bath management in order to keep the bath composition at the targeted values. As the galvanizing bath is saturated in iron, the main parameter to be controlled is the bath Al content, highly sensitive to Al-uptake by the inhibition layer. Therefore, a fine knowledge of the nature of this layer would facilitate the management of industrial galvanizing baths.

The facts presented hereinabove highlight the need to study this inhibition interfacial layer in detail, especially since this topic still remains controversial with regard to the exact nature of the intermetallic compounds that compose it.

With the composition chosen, the GA baths are composed of a ternary Al-Fe-Zn liquid phase in thermodynamic equilibrium with an intermetallic compound rich in iron and zinc, the δ phase[3–5] (measured composition of about 2.8 wt pct Al, 9.0 wt pct Fe and 88.2 wt pct Zn[6]). Very few authors have suggested that the GA inhibition layer could be composed of this thermodynamically stable δ phase and none of them has provided experimental evidence of the presence of this phase within its structure.[7–9] Most researchers have supported that this layer is mainly composed of metastable $Fe_2Al_5Zn_x$ $(0 < x < 1)$.[2,10–15] Some of them have reported the transient presence of other metastable phases, like $FeAl_3$[10,11,13,15] and $FeAl_2$,[11] in coexistence with $Fe_2Al_5Zn_x$. A biphasic interfacial layer composed of $Fe_2Al_5Zn_x$ with δ on its top was also reported.[16] Metastable epitaxial ζ ($FeZn_{13}$ containing less than 1 wt pct Al[4]) rod crystals may also appear, especially for low bath Al contents in the GA domain (slightly higher than 0.1 wt pct), together with the inhibition layer.[8,9,17,18] As can be seen, studies concerning the nature of the inhibition layer for GA coatings are few and the conclusions are very different from one study to another.

The purpose of the work presented here is first to precisely analyze the nature of the inhibition layer, then to provide theoretical tools based on thermodynamics and to propose reactions mechanisms to explain the results obtained.

The work is divided into the following stages:

(1) In the first stage, a precise characterization of the inhibition layer formed on steel samples galvanized in industrial conditions was performed;
(2) In the second stage, key mechanisms accounting for the formation of this layer will be proposed.

II. EXPERIMENTAL PROCEDURE

A. Materials

Two commercial Titanium-stabilized Interstitial-Free (*Ti-IF*) steels A and B have been selected for the present study. Their chemical composition is presented in Table I. The analysis was performed by means of Combustion and Infrared Detection for N (EMGA 620 W from Horiba) and Spark-Optical Emission Spectrometry (Spark-OES, SpectroLab M10 from Spectro) for the other elements in ArcelorMittal laboratories. The compositions of both steels are very similar. The thicknesses of steels A and B are equal to 0.80 and 0.74 mm, respectively.

Steels A and B were galvanized in industrial baths with different Al contents (0.112 and 0.128 wt pct Al) and saturated in iron. The operating conditions used to galvanize both steels are depicted in Table II.

Our aim was to study the formation of the inhibition layer under galvannealing conditions. Industrially, the galvannealing coating is heated to about 530 °C after the exit of the bath. During this heat treatment, the inhibition layer disappears completely and the final coating is composed only of thick Fe-Zn compounds. For this reason, the inhibition layer formed in galvannealing baths is generally studied in laboratory devices. To prove that our results are representative of industrial practice, we have chosen to work on steels galvanized in a continuous hot-dip galvanizing line as described above. To this end, the operating conditions have been defined in such a way as to maintain the integrity of the inhibition layer, *i.e.*, with the galvannealing furnace offline. The studied microstructures were then representative of the reactions mechanisms taking place in the molten metal bath.

The disadvantage of this type of approach is that we are dependent on industrial conditions. We chose two process windows that were as similar as possible. Both commercial steels belong to the same family, namely low-alloyed Titanium-stabilized Interstitial-Free steels. Their behavior is known to be the same with regard to immersion in liquid zinc.[2] The process window for industrial galvannealing conditions in the liquid metal bath is narrow and very well described by the two conditions examined (Table II). The influence of differences in galvanizing conditions, namely bath temperature, bath Al content and immersion time will be discussed later (Sections IV–A–2 and IV–A–3).

Table I. Average Chemical Composition ($\times$ 10^{-3} Wt Pct) of the Two Commercial *Ti-IF* Steels Studied

Steel	C	Mn	P	S	N	Si	Cu	Ni	Cr	Sn	Nb	Mo	B	Ti	Al
A	1.6	103	11	6	3.4	9	13	17	14	2	< 2	< 2	< 0.3	53	39
B	2.7	113	9	8	2.3	4	18	14	20	6	< 2	2	< 0.3	67	46

Table II. Process Data Used to Galvanize Both Steels

Steel	v (m/min)*	w_{Al} (Wt Pct)**	w_{Fe} (Wt Pct)**	T_{bath} (°C)[†]	L_{im} (m)[‡]	t_{im} (s)[$]	$e_{coating}$ (μm)[¶]
A	120	0.112 ± 0.004	0.027 ± 0.002	450 ± 2	2.7	1.4	5
B	130	0.128 ± 0.002	0.029 ± 0.001	460 ± 2	4.0	1.9	9

*Line speed.
**Bath Al and Fe content.
[†]Bath temperature.
[‡]Immersion length.
[$]$t_{im} = L_{im}/v$.
[¶]Zn coating thickness.

B. Experimental Techniques

1. Sample preparation techniques

a. Sample preparation techniques for surface characterization Specimens for surface characterization were cut into 32 mm diameter disks and submitted to a controlled electrochemical dissolution protocol in order to remove Zn and Fe-Zn phases selectively. The electrochemical cell used for these dissolutions was composed of three electrodes: a standard calomel electrode (SCE) used as reference electrode, a Pt counter electrode used as cathode and the sample to be dissolved (working electrode) used as anode. All the electrodes were linked to a VMP3 multi-channel potentiostat from BioLogic Science Instruments. The electrolyte used is an aqueous pH 4 solution composed of 200 g/L NaCl (Fisher Chemical), 40 g/L $ZnSO_4 \cdot 7H_2O$,[19] 27 g/L CH_3COONa, and 11 mL/L CH_3COOH (VWR BDH Prolabo). The electrochemical potentials to be imposed are -950 mV for Zn removal only and − 680 mV for Zn and Fe-Zn phases removal which would keep $Fe_2Al_5Zn_x$ at the sample surface if present. An extraction technique was then applied to the samples submitted to the electrochemical dissolution at − 680 mV in order to obtain thin $Fe_2Al_5Zn_x$ films for analysis in the transmission electron microscope (TEM). The extraction protocol is described in detail in Reference 20.

b. Sample preparation techniques for cross-section characterization Cross-section specimens for Scanning Electron Microscope (SEM) analysis were prepared by Ar ion beam cross-section polishing (CSP, *JEOL SM-09010*). Prior to this operation, a mechanical polishing step was performed on one side of the galvanized steel samples in order to reduce the sample thickness to around 400 μm. Ion beam polishing from the steel matrix towards the coating was then accomplished at an accelerating voltage of 6 kV and an ion beam current around 150 μA during a processing time of 3 hours. Cross-section thin foils for TEM analysis and tips for Atom Probe Tomography (APT) were prepared by Focused Ion Beam (FIB) technology (SII Nanotechnology Inc SMI 3050 TB for thin foils and FEI Helios 600 Nanolab for tips). Samples were previously submitted to an electrochemical dissolution at − 950 mV to remove the Zn overlay. A very thin Au (respectively, Ni) layer for thin foils (respectively, tips) was then deposited by means of a sputter coater (Balzers SCD050, respectively, Quorum Q150TS) on the sample surface for conductivity reasons. Once in the FIB device, a Pt layer was deposited on the sample surface in order to protect the foil. The milling operations were conducted with a Ga ion beam. The final dimensions of the foils (respectively, tips) are around 14 μm × 7 μm × 50 nm (respectively, 50 nm × 50 nm × 100 nm).

2. Sample characterization techniques

The CSP cross-section samples were analyzed by Energy Dispersive Spectroscopy (EDS, Bruker AXS XFlash 4010 SDD) in a SEM (JEOL JSM-7001F) with the purpose of characterizing the general structure of the inhibition layer.

In order to determine the nature of the phases present in the inhibition layer, the thin FIB foils and extracted films were analyzed by EDS (Bruker AXS XFlash 5030T SDD) and electron diffraction in a TEM (JEOL JEM-2100F) at an accelerating voltage of 200 kV.

The local composition of the inhibition layer was determined by APT (CAMECA LEAP 3000XHR) in voltage mode with a pulse fraction of 20 pct. During analysis, the temperature of the specimen was maintained at 70 K. APT data were reconstructed using the software IVAS 3.6.14 from CAMECA.

Interest was also given to the geometrical features of the inhibition layer for steels A and B. Their thicknesses and surface coverage, in the case of discontinuous layers, were determined by means of high resolution SEM and TEM micrographs obtained during the analysis of the CSP and FIB cross-section samples.

III. RESULTS

A. General Structure

SEM results obtained on the CSP samples (430 μm for steel A and 220 μm for steel B) show that the inhibition layer is composed of two different layers. The Al content in the bottom layer (in direct contact with the steel substrate) is higher than the Al content in the top layer (blue signal in Figure 1). This two-layer structure was also confirmed by EDS analysis of the FIB cross-sections performed in the TEM (Figure 2). In the case of steel A, galvanized in a Zn bath with 0.112 wt pct Al, the Al-rich layer is discontinuous (Figures 1, left and 2, top, whereas in the case of steel B, galvanized in a Zn bath with 0.128 wt pct Al, this layer is continuous (Figures 1, right and 2, bottom). For
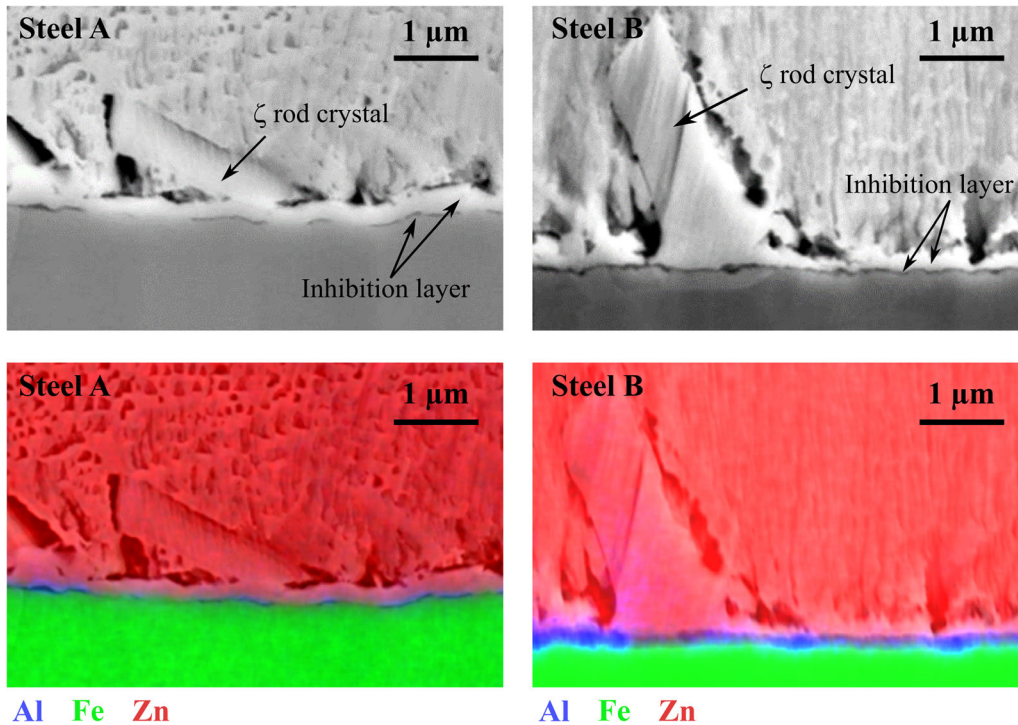
Fig. 1—Cross-section micrographs (top) and EDS mappings (bottom) performed in the SEM (Zn in red, Al in blue, and Fe in green) on the CSP samples prepared from steels A (left), galvanized in a Zn bath containing 0.112 wt pct Al, and B (right), galvanized in a Zn bath containing 0.128 wt pct Al. The inhibition layer is composed of two layers: a very thin Al-rich layer (discontinuous in the case of steel A and continuous in the case of steel B) covered with a thicker continuous Al-poor layer. Adapted from Ref. [20] (Color figure online).

both steels, ζ rod crystals are also present in agreement with the results reported in the literature.[7–9,17,18]

The average thickness of these two phases in the inhibition layer was estimated from measurements performed on the CSP and FIB samples (Table III). The thicknesses obtained are fairly the same in both steels: the bottom Al-rich layer is around 20 nm thick and the top Zn-rich layer around 200 nm thick.

Finally, the surface coverage of the Al-rich layer was estimated from the linear fraction occupied by this layer (ratio between the lengths of the interface between steel and the Al-rich layer and the total length of the interface for the CSP samples).[21] It was found to be around 52 pct for steel A and 88 pct for steel B.

B. Nature of the Inhibition Layer

1. Elemental analysis

The elemental composition of the two layers constituting the inhibition layer was determined by EDS analysis performed on the FIB cross-sections for the top layer and the extracted films for the bottom layer in the TEM (Table IV). The experimental results obtained for steels A and B are compared with the composition of δ and $Fe_2Al_5Zn_x$ involved in the thermodynamic equilibrium with α ferrite found in the literature[6] (compositions given under Table IV). Due to the shape of the ternary Al-Fe-Zn phase diagram (Figure 7), this composition is very close to the composition of δ and $Fe_2Al_5Zn_x$ involved in thermodynamic equilibria with the liquid phase.[4,6] The composition of the bottom

(respectively, top) layer corresponds to the composition of $Fe_2Al_5Zn_x$ (respectively, δ).

2. Crystal structure

The crystal structure of the two layers constituting the inhibition layer was determined by electron diffraction performed on the FIB cross-sections for the top layer and the extracted films for the bottom layer in the TEM. The diffraction patterns obtained are presented in Figures 3 and 4.

In Figure 3, the experimental electron diffraction patterns obtained for the top layer are compared with the electron diffraction pattern calculated (colored circles) for the δ phase (hexagonal lattice, space group P6₃/mmc, lattice parameters $a = b = 1.28297$ nm, $c = 5.72860$ nm[22]). The theoretical electron diffraction pattern was simulated using JEMS software[23] and the CIF file no. 192095 for $Fe_{13}Zn_{126}$ from the Inorganic Crystal Structure Database ICSD.[24,25] The measured distances and angles of the top layer are characteristic of the δ phase, in the [3 1 1] and [4 2 1] incidence electron planes for the examples chosen. It should be noted that a few reflections are not predicted by the simulated electron diffraction pattern (e.g., black stars). This may be due to the presence of Al in the δ phase (Table IV). The influence of Al is not known and is not taken into account in the cell structure of δ used for the simulation.[22] However, this is more likely due to the double diffraction reflections. Since our objective was to determine the exact nature of the compounds and not to measure precise lattice parameters, we chose a
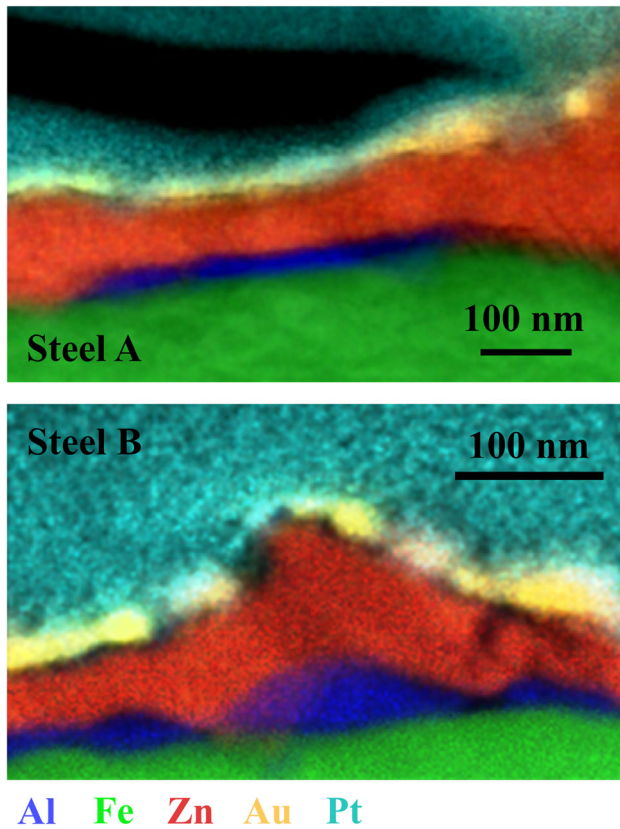
Fig. 2—Cross-section micrographs and EDS mapping performed in the TEM (from bottom to top, Fe in green, Al in dark blue, Zn in red, Au in yellow, and Pt in light blue) on the FIB foils prepared from steels A (top), galvanized in a 0.112 wt pct Al-containing Zn bath, and B (bottom), galvanized in a 0.128 wt pct Al-containing Zn bath. The inhibition layer is in both cases composed of two layers (Au and Pt comes from the preparation of the FIB foils) (Color figure online).

Table III. Estimation of the δ (Top Layer) and $Fe_2Al_5Zn_x$ (Bottom Layer) Average Thicknesses from Measurements Performed on the CSP and FIB Micrographs

Steel	Top Layer (nm)*	Bottom Layer (nm)**
A	197 ± 61	24.1 ± 3.8
B	248 ± 77	23.2 ± 11.0

*Estimated from the SEM observations of the CSP samples (105 measurements for steel A and 66 for steel B).
**Estimated from the TEM observations of the FIB samples (9 measurements for steel A and 15 for steel B).

pseudo-convergent beam electron diffraction (CBED) approach to obtain a single compound per diffraction pattern to facilitate their analysis. But this mode, where the transmitted beam is focused and intense, favors the defect of double diffraction. Calculations with JEMS software including double diffraction predict that the double diffraction spots, if they exist, are found at the locations indicated by the black stars in Figure 3.

In Figure 4, the experimental electron diffraction patterns obtained for the bottom layer are compared with the electron diffraction pattern calculated (colored circles) for the Fe_2Al_5 phase (orthorhombic lattice, space group Cmcm, lattice parameters $a = 0.76559$ nm, $b = 0.64154$ nm, $c = 0.42184$ nm[26]). The theoretical electron diffraction pattern was simulated using JEMS software[23] and the CIF file no. 105132 for $Fe_2Al_{5.6}$ from the Inorganic Crystal Structure Database ICSD.[24,25] The measured distances and angles of the bottom layer are characteristic of the Fe_2Al_5 phase, in the [3 1 2] and [0 0 1] incidence electron planes for the examples chosen. The influence of Zn is not known and is not taken into account in the cell structure of Fe_2Al_5 used for the simulation.[26] However, it seems that Zn has little influence on the electron diffraction pattern.

It can therefore be confirmed that the inhibition layer formed on steels A and B is composed of a very thin layer of the $Fe_2Al_5Zn_x$ phase on the steel substrate and a thicker layer of the δ phase on top of it. The main difference observed in the structure of both inhibition layers is the discontinuity of the thin layer of $Fe_2Al_5Zn_x$ in the case of steel A. This microstructure is in agreement with the one proposed by Dionne et al.[16] deduced from EDS analysis performed in the TEM.

3. Concentration profiles measured by APT

a. Complementary analyses were performed by means of APT (Figure 5) 1D concentration profiles were obtained in the direction perpendicular to the steel surface. The results are similar for both steels (Figure 5(a)) and in good agreement with the results shown before. The inhibition layer is confirmed to be constituted by a two-layered structure. The mean composition of each layer was calculated from the quantitative analysis of several tips (top layer: 2 tips for steel A and 4 tips for steel B; bottom layer: 1 tip for each steel). The mean composition of the top layer is close to the composition of the δ phase (Table IV). The mean composition of the bottom layer is close to but slightly different from the composition of $Fe_2Al_5Zn_x$ (the stoichiometry estimated by APT measurements is Fe/Al = 0.54 compared to 0.4 in Reference 6, Table IV). This difference could be attributed either to a peak overlap between $^{27}Al^+$ and $^{54}Fe^{2+}$ around the 27 amu mass or to inaccuracy in the composition measurement for a few nm-thick layer. Peak overlap plays a minor role since the $^{27}Al^+$ and $^{54}Fe^{2+}$ peaks are minor peaks in the mass spectrum.

Interface broadening is usually observed on the depth profiles measured by APT even if the interface is atomically sharp and perfectly flat. This interface broadening may have several causes, including classical phenomena such as interface roughness and information depth, but also phenomena related to atom probe such as preferential evaporation, differences in the evaporation field, or other causes linked to data analysis (positioning of the sub-volume, binning, etc.).[27] The interface broadening linked to APT can be estimated to be of a few nm.[27,28] In Figure 5(c), the thickness of $Fe_2Al_5Zn_x$ is in the order of 4 to 5 nm and the measurement of the Al, Fe and Zn concentrations in $Fe_2Al_5Zn_x$ can be affected by both interfaces, namely δ/

$Fe_2Al_5Zn_x$ and $Fe_2Al_5Zn_x$/steel. The composition gradient observed in these interfaces is mainly a consequence of the interface broadening and does not mean that the compositions of δ and $Fe_2Al_5Zn_x$ are not constant up to the vicinity of the interfaces. It was also discovered that small particles of about 20 nm in size are present in the inhibition layer of both steels. These particles are preferentially located in the δ phase and are rich in Fe (Figures 5(b) and (d)). Their mean composition calculated from the quantitative analysis of 3 tips (1 for steel A and 2 for steel B) is 12.8 ± 2.9 wt pct Al, 68.1 ± 3.1 wt pct Fe, 19.1 ± 5.7 wt pct Zn (or 22.8 ± 5.2 mol pct Al, 58.4 ± 2.7 mol pct Fe, 14.0 ± 4.2 mol pct Zn). This phase could therefore be Fe_3Al-containing Zn.

IV. DISCUSSION

The main results of our study will now be discussed: *i.e.*, (i) the inhibition layer is composed of $Fe_2Al_5Zn_x$ and δ (Section IV–A); (ii) small precipitates with a stoichiometry corresponding to Fe_3Al-containing Zn were also found in the δ phase (Section IV–B).

A. *Formation of $Fe_2Al_5Zn_x$ and δ*

1. *Thermodynamics of the inhibition layer*

The final microstructure of the inhibition layer can be visualized with the aid of the so-called diffusion paths[29,30] in the Al-Fe-Zn ternary phase diagram.[7–9,11] The diffusion path is a line representing the locus of the average composition in planes parallel to the original steel/liquid zinc interface, throughout the diffusion zone. If two phases are separated by a planar interface that is in local equilibrium, the diffusion path crosses the single-phase regions and the two-phase region parallel to a tie line. The composition of the phases in contact at the interface is given by the tie-line ends and the tie line in question is represented by a dashed-dotted line (in agreement with the conventions in Reference 29).

Figure 6 is a schematic representation of the Al-Fe-Zn ternary phase diagram at 450 to 460 °C.[3] This representation is not at scale. The different phases' regions are larger than in reality (Figure 7) to facilitate the understanding of the diffusion paths presented. The regions that are not useful for understanding the formation of $Fe_2Al_5Zn_x$ and δ were deliberately excluded from this representation (*e.g.*, FeAl$_3$-Zn, Fe_3Al and FeAl). The formation of Fe_3Al particles will be discussed in Section IV–B–1.

The inhibition layer formed in the galvanizing bath on steel B consists of two layers with planar interfaces: steel/$Fe_2Al_5Zn_x$/δ/liquid zinc bath (Figures 1, right and 6, top right). This microstructure can be represented on the isothermal section by the diffusion path 1 between point b (representing the liquid phase in the galvanizing bath) and the Fe corner (Figure 6, bottom). In this case, the diffusion path is equivalent to the concentration profile that could be measured in the direction perpendicular to the steel surface. The first part of the diffusion path from point b indicates that the mass balance requires a slight depletion of the bath in aluminum (the diffusion path therefore crosses the straight line joining the terminal compositions of the diffusion couple Fe and b[29,30]). In the single-phase regions, the diffusion path is generally not a straight line. The shape of the diffusion path is related to four diffusion coefficients D_{ij}^k in each phase defined as diffusion coefficient relating flux of component i (*i.e.*, Zn and Al) to concentration gradient of component j (*i.e.*, Zn and Al) in solvent k (*i.e.*, α-Fe, $Fe_2Al_5Zn_x$ or δ). These four diffusion coefficients are not available for the single-phase regions of the Al-Fe-Zn ternary phase diagram. We then decided to approximate the diffusion path in single-phase regions by a straight line.

In the case of steel A, $Fe_2Al_5Zn_x$ is discontinuous (Figure 1, left) and the inhibition layer locally consists of one or two phases with planar interfaces: steel/δ/liquid zinc or steel/$Fe_2Al_5Zn_x$/δ/liquid zinc (Figure 6, top left). These local microstructures can be described by the concentration profiles 2 and 1, respectively, on the isothermal section (blue and orange solid and dotted-dashed lines, Figure 6, bottom). In some places, the steel/inhibition layer interface is composed of three phases at equilibrium (steel, δ, $Fe_2Al_5Zn_x$) and one can think that there may be a concentration gradient of Al, Fe and Zn at the interface between Fe and $Fe_2Al_5Zn_x$ or δ, towards the triple points where the three phases coexist (blue and orange arrows and dotted lines 1 and 2, Figure 6, top left and bottom). The corresponding diffusion path can be represented by the diffusion path 3 with the three-phase equilibrium on the steel side and the two-phase δ/$Fe_2Al_5Zn_x$ equilibrium on the coating side (black dotted-dashed line, Figure 6, bottom).

As a conclusion, the microstructures observed for the inhibition layer can be described with diffusion paths drawn on the Al-Fe-Zn ternary isothermal section. This suggests that all interfaces of the inhibition layer formed on both steels are at thermodynamic equilibrium.

2. *Reaction mechanisms*

a. General mechanisms A general agreement exists in the literature concerning the mechanisms accounting for the formation of the inhibition layer: at the moment when the steel sheet penetrates the galvanizing bath, the iron concentration increases at the steel/liquid zinc interface due to the iron dissolution. This leads to the establishment of an iron supersaturation, which is the driving force for nucleation and growth of the inhibition layer.[1,2] The immersion time of the steel strips in the galvanizing baths is of the order of a few seconds (Table II). As was shown in References 31 and 32 for a GI bath (0.2 wt pct Al) at 460 °C, 90 pct of the thickness of the inhibition layer is formed very rapidly (less than 0.4 second) and depends on the kinetics of iron dissolution and intermetallic compound growth and on liquid state diffusion, the remaining 10 pct of the thickness is formed when growth is controlled by solid-state diffusion. This behavior can be explained by a high initial dissolution rate of iron when the steel strip enters the galvanizing bath (0.3 g/m^2 in 0 second[32]). In GA baths (0.12 wt pct Al), the reaction

Table IV.   Quantitative Analysis of the Two Sublayers Constituting the Inhibition Layer: EDS Analysis Performed in the TEM Obtained for Steels A, Galvanized in a Zn Bath Containing 0.112 Wt Pct Al, and B, Galvanized in a Zn Bath Containing 0.128 Wt Pct Al; Mean Composition Obtained by Means of APT (Using Tips from Steels A and B)

Elements	Steel A (EDS-TEM)		Steel B (EDS-TEM)		APT	
	Top Layer	Bottom Layer	Top Layer	Bottom Layer	Top Layer	Bottom Layer
Al (Wt Pct)	2.7 ± 0.1	44.3 ± 1.4	2.7 ± 0.1	49.3 ± 1.5	1.3 ± 0.3	39.4 ± 3.1
Fe (Wt Pct)	12.0 ± 0.4	36.4 ± 1.2	11.1 ± 0.4	36.7 ± 1.1	9.5 ± 1.7	43.8 ± 1.5
Zn (Wt Pct)	85.3 ± 2.6	19.3 ± 0.7	86.2 ± 2.6	14.0 ± 0.5	89.2 ± 1.7	16.7 ± 1.8
Al (Mol Pct)	6.2 ± 0.4	63.4 ± 4.1	6.2 ± 0.4	67.7 ± 4.1	3.0 ± 0.7	56.8 ± 4.5
Fe (Mol Pct)	13.3 ± 0.9	25.2 ± 1.6	12.3 ± 0.8	24.4 ± 1.5	9.1 ± 1.6	30.5 ± 1.0
Zn (Mol Pct)	80.6 ± 5.0	11.4 ± 0.8	81.5 ± 5.0	7.9 ± 0.5	85.8 ± 1.8	10.0 ± 1.1

The composition of the bottom (respectively, top) layer corresponds to the composition of the $Fe_2Al_5Zn_x$ (respectively, δ).[6] The measurements in the table can be compared to the composition of two intermetallic compounds (Chen *et al.*[6]): δ (2.8 ± 0.3 Wt Pct Al, 9.0 ± 0.6 Wt Pct Fe, 88.2 ± 0.7 Wt Pct Zn) and $Fe_2Al_5Zn_x$ (43.1 ± 1.1 Wt Pct Al, 36.0 ± 0.6 Wt Pct Fe, 20.9 ± 1.7 Wt Pct Zn).

mechanisms and kinetics are the same. The weight of iron dissolved per unit area is about 0.5 g/m^2 under similar galvanizing conditions as the ones employed here (immersion for 2 seconds in a Zn bath containing 0.12 wt pct Al at 465 °C[33]). This value is larger than the weight of iron per unit area in the inhibition layer, estimated at 0.15 g/m^2*. Therefore, the iron in the

---

*The inhibition layer was found to be composed of $Fe_2Al_5Zn_x$ (about 20 nm thick) and δ (about 200 nm thick) (Table 3). With the densities taken in the CIF files already used to index the electron diffraction patterns (Section 3.2.2), namely N° 105132 for $Fe_2Al_{5.6}$ (4210 kg m^{-3}) and N° 192095 for $Fe_{13}Zn_{126}$ (7290 kg m^{-3}), the weight of iron per unit area of inhibition layer is 0.15 g m^{-2}.

---

inhibition layer mainly comes from the initial iron dissolution and the formation of the inhibition layer is mainly related to reaction kinetics and liquid state diffusion.

b. Inhibition layer growth   The inhibition layer is composed of $Fe_2Al_5Zn_x$ covered by δ (Section III). The question now is which intermetallic compound, $Fe_2Al_5Zn_x$ or δ, is first formed after the initial step of iron dissolution.   The experimental liquidus in the Zn-rich corner of the Al-Fe-Zn ternary phase diagram[4,5] corresponds to the equilibrium between the liquid phase and δ when the Al content is in the range [0.10, 0.134 wt pct][4] ([0.07, 0.134 wt pct] in Reference 5) and $Fe_2Al_5Zn_x$ when the Al content is higher than 0.134 wt pct, regardless of temperature (450 or 460 °C). Therefore, δ is the equilibrium intermetallic compound whereas $Fe_2Al_5Zn_x$ is metastable in the galvanizing baths containing 0.112 and 0.128 wt pct Al studied here (Table II).   If δ were formed first, thermodynamic equilibrium could be reached at all the interfaces, *i.e.*, Fe/δ/liquid Zn (diffusion path 2, Figure 6). The subsequent nucleation and growth of $Fe_2Al_5Zn_x$ in between ferrite and δ by solid-state diffusion is less likely than the growth of δ by consumption of the Fe supersaturation.   It can be deduced that metastable $Fe_2Al_5Zn_x$ is probably formed first on the steel surface instead of stable δ phase. $Fe_2Al_5Zn_x$ nucleation could be favored

by epitaxial relationships with ferrite, already reported by different authors[2,9,34,35]:

$(3\bar{1}1)_{Fe_2Al_5}//(110)_{Fe_\alpha}$ and possibly $(221)_{Fe_2Al_5}//(110)_{Fe_\alpha}$;

$(1\bar{3}0)_{Fe_2Al_5}//(101)_{Fe_\alpha}$ and $[001]_{Fe_2Al_5}//[\bar{1}01]_{Fe_\alpha}$;

$(001)_{Fe_2Al_5}//(011)_{Fe_\alpha}$ and $[\bar{1}30]_{Fe_2Al_5}//[\bar{1}00]_{Fe_\alpha}$;

$(001)_{Fe_2Al_5}//(0\bar{1}1)_{Fe_\alpha}$, $(1\bar{1}0)_{Fe_2Al_5}//(2\bar{1}\bar{1})_{Fe_\alpha}$

and $[110]_{Fe_2Al_5}//[111]_{Fe_\alpha}$.

However, $Fe_2Al_5Zn_x$ is not in thermodynamic equilibrium with liquid zinc. With the subsequent nucleation and growth of the δ phase, thermodynamic equilibrium is reached at all the interfaces of the system, *i.e.*, Fe/$Fe_2Al_5Zn_x$/δ/liquid zinc (Figure 6, path 1). The δ phase growth is mainly due to the consumption of the iron supersaturation.   This reaction mechanism, namely $Fe_2Al_5Zn_x$ formation before δ, was already proposed by Yamaguchi and Hisamatsu[15] in 1979, deduced from the shape of the ternary Al-Fe-Zn phase diagram. They explained that δ nucleation is caused by an Al depletion due to the formation of $Fe_2Al_5Zn_x$. However, the characteristic diffusion length of Al in liquid Zn is high enough to ensure that the growth of $Fe_2Al_5Zn_x$ is not stopped by a lack of Al (Supplementary Materials A). Chen *et al.*[10] have proposed another mechanism for the formation of the Al-rich layer: $FeAl_3$ appears first and forms a continuous layer of small crystals of a few tens of nm. $FeAl_3$ is then transformed into Fe_2Al_5 by solid-state reactive diffusion of Fe and Al. This mechanism was proposed on the basis of the EBSD analysis, which mainly detected $FeAl_3$ up to 2 seconds of galvanizing and then Fe_2Al_5 (after 5 seconds). This means that the transformation of $FeAl_3$ into Fe_2Al_5 would take about 3 seconds. To assess the relevance of this mechanism, the characteristic time τ required to transform the $FeAl_3$ layer into Fe_2Al_5 can be estimated and compared to these 3 seconds: $\tau = e^2/D$ where e is the thickness of the $FeAl_3$ layer (assumed to be 20 nm, Table II) and D is the diffusion coefficient of Fe or Al or the interdiffusion coefficient in $FeAl_3$. To our knowledge, there is no measurement of the diffusion coefficients in $FeAl_3$. But measurements can be found
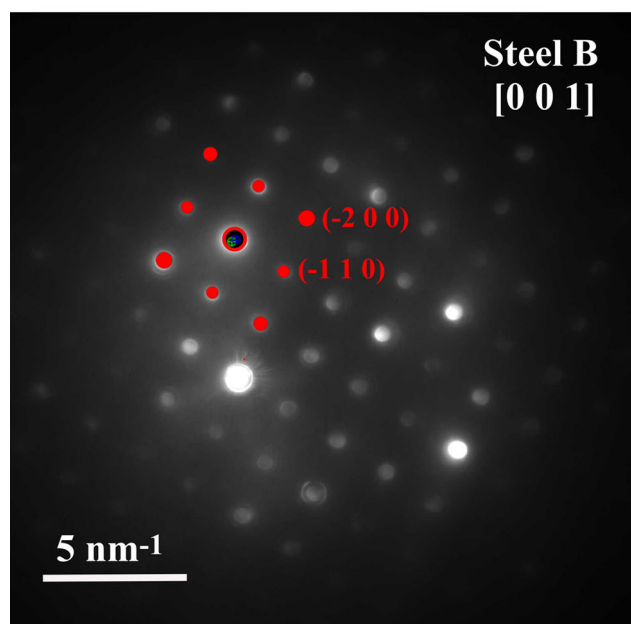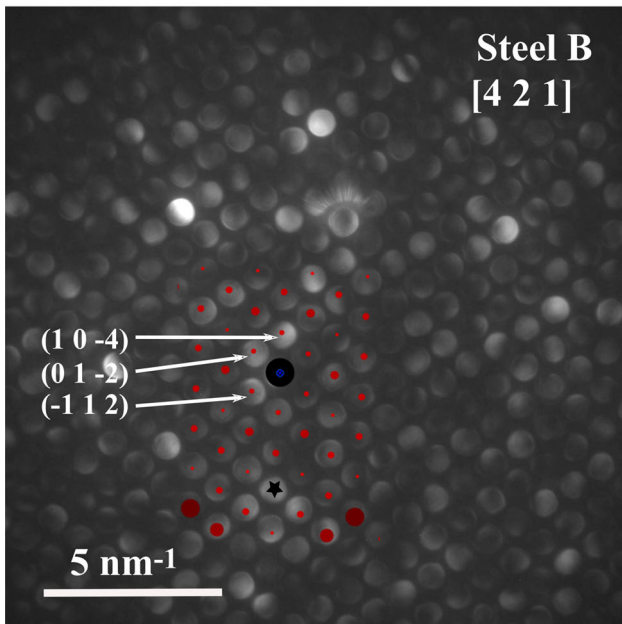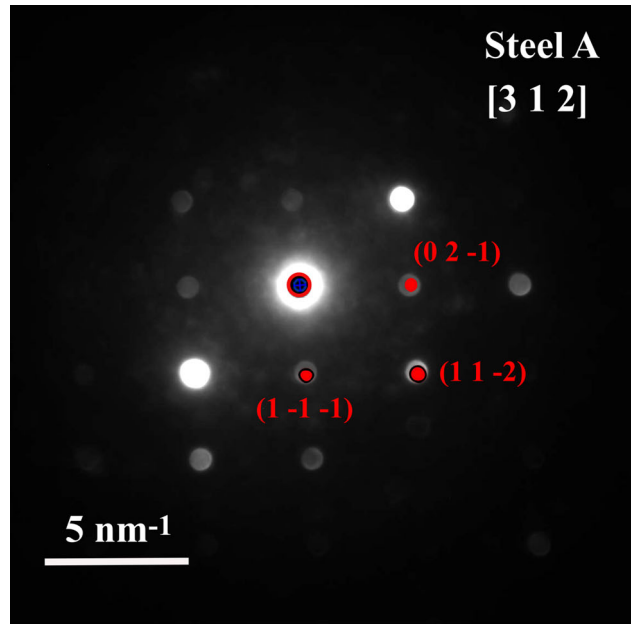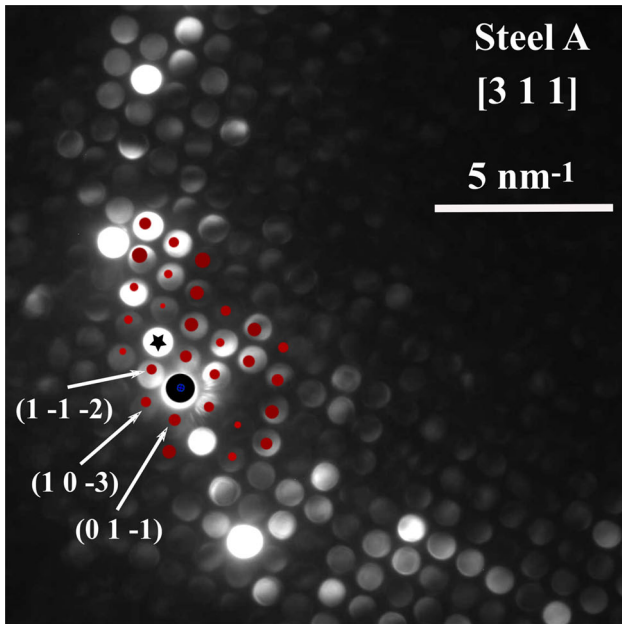
Fig. 3—Diffraction patterns of the Zn-rich phase of the inhibition layers of the FIB foils prepared from steels A (top), galvanized in a 0.112 wt pct Al-containing Zn bath, and B (bottom), galvanized in a 0.128 wt pct Al-containing Zn bath. The experimental electron diffraction patterns are characteristic of the δ phase (in the [3 1 1] and [4 2 1] incidence electron planes for the examples chosen). Missing diffraction spots in the theoretical diffraction pattern (red points), indicated by black stars, are predicted by JEMS calculations by including double diffraction (Color figure online).

Fig. 4—Diffraction patterns of the Al-rich phase of the inhibition layers extracted from steels A (top), galvanized in a 0.112 wt pct Al-containing Zn bath, and B (bottom), galvanized in a 0.128 wt pct Al-containing Zn bath. The experimental electron diffraction patterns are characteristic of the $Fe_2Al_5Zn_x$ phase (in the [3 1 2] and [0 0 1] incidence electron planes for the examples chosen) (Color figure online).

for Fe_2Al_5 at temperatures above 550 °C: these measurements extrapolated to 460 °C allow to estimate the diffusion coefficient of Fe in Fe_2Al_5 at 5×10^{-17} m^2/s[45] and the interdiffusion coefficient in Fe_2Al_5 at 2.7×10^{-18} m^2/s.[46] As in the Fe/Al diffusion couples only Fe_2Al_5 is formed while $FeAl_3$ is also thermodynamically stable, one of Naio and Kajihara's

conclusions[46] is that diffusion in $FeAl_3$ is much slower than in Fe_2Al_5. The characteristic time τ required to transform the 20 nm-thick $FeAl_3$ layer into Fe_2Al_5 is therefore higher than the characteristic time calculated using the diffusion coefficients in Fe_2Al_5, i.e., 8 or 140 seconds and of course also higher than 3 seconds. Finally, we did not include $FeAl_3$ formation in the proposed mechanism for the following reasons: (i) the
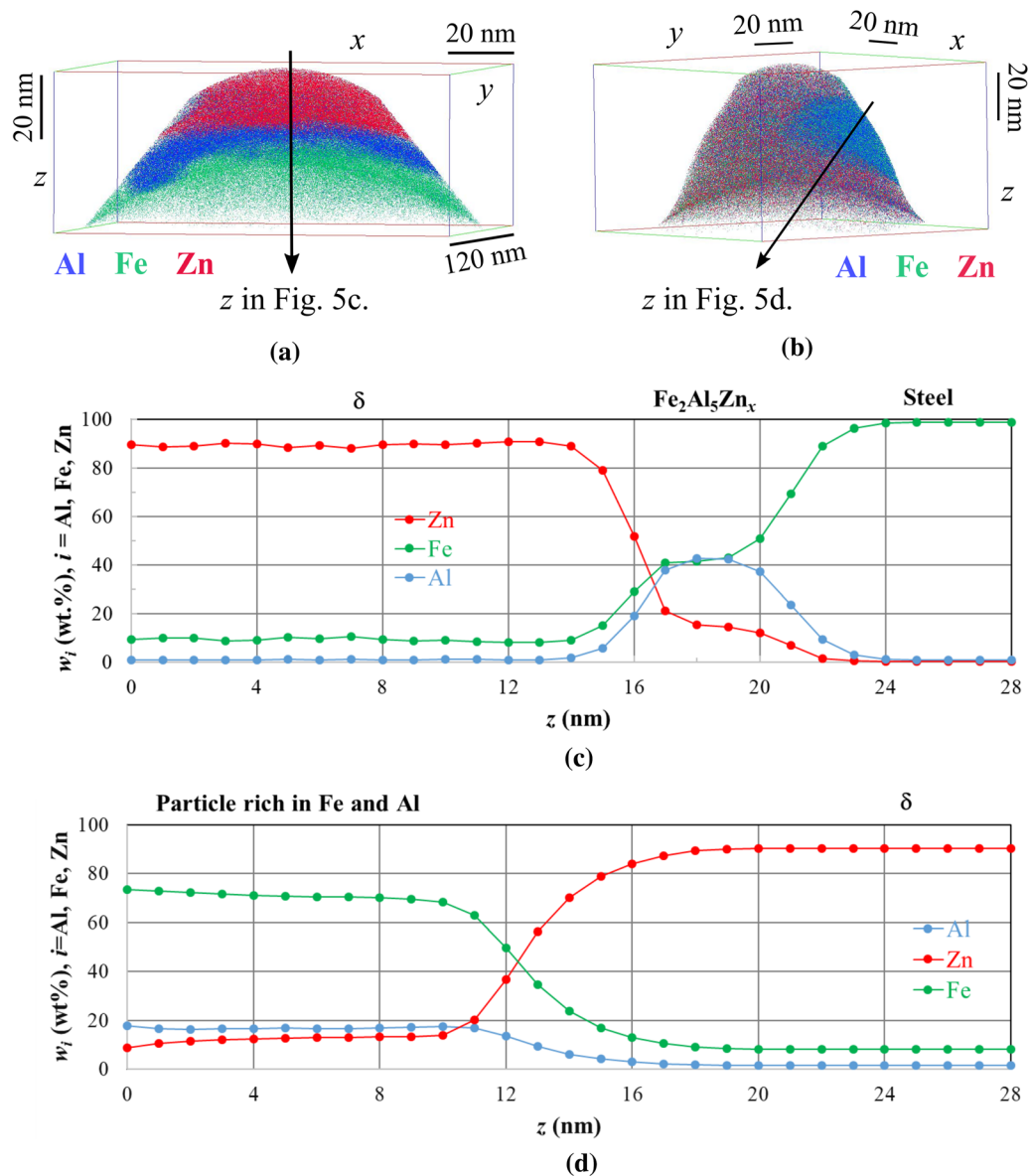
Fig. 5—Composition of the inhibition layer measured by APT: (*a*) The inhibition layer is a two-layered structure, with a very thin Al-rich layer covered with a thicker Zn-rich layer; (*b*) small particles rich in Fe are present in the inhibition layer; (*c*) and (*d*) Al, Fe and Zn concentration profiles measured in the directions indicated by the arrows in (a) and (b), respectively (Color figure online).

characteristic time τ is greater than 3 seconds, (ii) the presence of $FeAl_3$ in the inhibition layer was measured only by EBSD (the thickness of the inhibition layer being only a few tens of nm, EBSD is not the most appropriate technique to analyze its nature), (iii) we did not find $FeAl_3$ in our analyses. In addition, the Al present in the interfacial layer (called Al-uptake) is estimated at about 77 mg/m^2 (considering a thickness of 20 nm of $Fe_2Al_5Zn_x$ and 200 nm of δ (Table III) with compositions in Table IV and densities in Section IV–A–2). This Al-uptake value is in very good agreement with the chemical analysis performed by Chen *et al.* (Figure 13b in Reference 10) at 460 °C for a reaction time of 7 seconds (2 seconds in bath and about 5 seconds of cooling before solidification in our case). The chemical analysis of the interfacial layer presented by Chen is therefore in good agreement with the microstructure of the inhibiting layer presented here, *i.e.*, a double layer composed of $Fe_2Al_5Zn_x$ and δ.

3. Effect of the galvanizing conditions

Steels A and B were galvanized in iron-saturated zinc baths with different aluminum contents and temperatures: 0.112 wt pct Al and 450 °C for steel A and 0.128 wt pct Al and 460 °C for steel B. (Table II).

The composition of the galvanizing baths used for steels A and B is located in the liquid—δ domain. The Al content range of this two-phase region hardly depends on temperature: [0.10, 0.134 wt pct][4] ([0.07, 0.134 wt pct] in Reference 5) regardless of temperature (450 or 460 °C). Therefore, the small difference of 10 °C in temperature between the two conditions tested here (450 and 460 °C) is not expected to change the chemical nature of the inhibition layer.
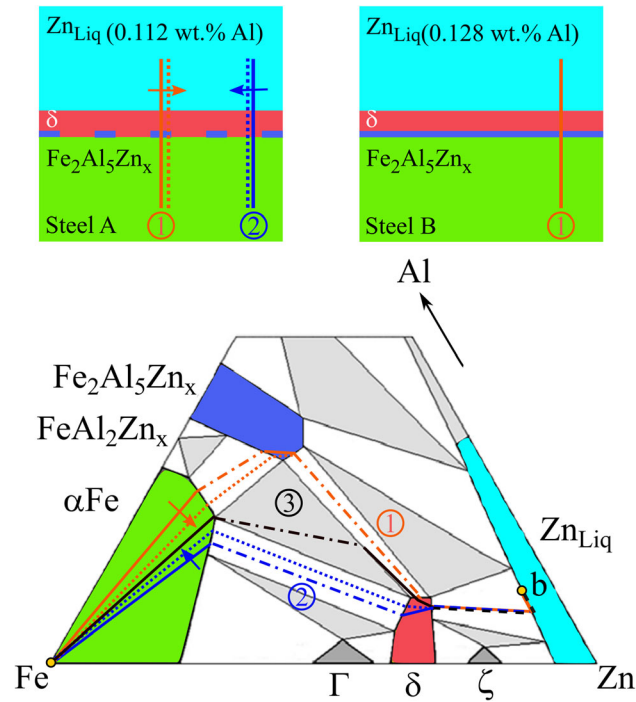
Fig. 6—Final microstructure of the inhibition layer (top) visualized by diffusion paths in the Al-Fe-Zn ternary phase diagram at 450 to 460 °C (bottom: this representation is not at scale and the different phases' regions are larger than in reality (Fig. 7) to facilitate the understanding of the diffusion paths presented): local concentration profiles 1 and 2 and diffusion path 3 for steel A and diffusion path 1 for steel B (Color figure online).

Fig. 7—Al-Fe-Zn ternary diagram proposed by Tang[3,4] compared with experimental points from the literature in the Fe-rich corner.[6,11,38,40,44] The mean composition of the small particles found in the δ phase of the inhibition layer (small stars) corresponds to Fe₃Al-containing Zn (blue line). Adapted from Ref. [3] (Color figure online).

Due to initial dissolution, the concentration of iron at the interface between steel and liquid zinc increases and exceeds the saturation limit with respect to δ (stable compound) or Fe₂Al₅Znₓ (metastable compound). This supersaturation is the driving force for heterogeneous nucleation of δ or Fe₂Al₅Znₓ on the steel surface. The Gibbs free energy $\Delta G_{\text{nucl}}^{\text{comp}}$ of formation of a nuclei from the supersaturated bath is given by Reference 36:

$$\Delta G_{\text{nucl}}^{\text{comp}} = \Delta G_{\text{vol}}^{\text{comp}} + \Delta G_{\text{surf}}^{\text{comp}} \qquad [1]$$

where *comp* stands for intermetallic compound (δ or Fe₂Al₅Znₓ), $\Delta G_{\text{vol}}^{\text{comp}}$ is the Gibbs free energy change for the formation of the intermetallic compound from the supersaturated liquid phase and $\Delta G_{\text{surf}}^{\text{comp}}$ is the Gibbs free energy due to the creation of new interfaces, namely *comp*/liquid Zn and *comp*/steel. Therefore,

$$\Delta G_{\text{vol}}^{\text{comp}} < 0 \text{ and } \Delta G_{\text{surf}}^{\text{comp}} > 0 \qquad [2]$$

In the case of steels A and B studied here, the first intermetallic compound to be formed will be the one with the lowest Gibbs free energy of formation $\Delta G_{\text{nucl}}^{\text{comp}}$. As δ is the intermetallic compound in equilibrium with the liquid phase in both cases,

$$\Delta G_{\text{vol}}^{\delta} < \Delta G_{\text{vol}}^{\text{Fe}_2\text{Al}_5\text{Zn}_x}, \qquad [3]$$

However, as shown in Section IV–A–2, Fe₂Al₅Znₓ is probably formed first. This means that the wetting of αFe by Fe₂Al₅Znₓ is better than the one by δ, probably due to epitaxial relationships between Fe₂Al₅Znₓ and αFe,[2,9,10,34,35] leading to:

$$\Delta G_{\text{surf}}^{\delta} > \Delta G_{\text{surf}}^{\text{Fe}_2\text{Al}_5\text{Zn}_x} \qquad [4]$$

and

$$\Delta G_{\text{nucl}}^{\delta} > \Delta G_{\text{nucl}}^{\text{Fe}_2\text{Al}_5\text{Zn}_x} \qquad [5]$$

For steel A, the Fe₂Al₅Znₓ layer is discontinuous. The Al content in the bath (0.112 wt pct) is lower than in the case of steel B (0.128 wt pct) where the Fe₂Al₅Znₓ layer was observed to be continuous. The liquid phase is in equilibrium with δ when the Al content is in the range [0.10, 0.134 wt pct] and Fe₂Al₅Znₓ when the Al content is higher than 0.134 wt pct. When the Al content is lowered, $\Delta G_{\text{vol}}^{\text{Fe}_2\text{Al}_5\text{Zn}_x}$ becomes less negative. This is the reason why, in the case of steel A, the nucleation of Fe₂Al₅Znₓ becomes more difficult and the final Fe₂Al₅Znₓ layer is discontinuous.

B. *Other Phases in the Inhibition Layer*

1. *Small particles of Fe₃Al-containing Zn*

a. Are the Fe₃Al particles in thermodynamic equilibrium? Small particles rich in Fe are present in the δ phase of the inhibition layer formed on both steels (Figure 5(b)). The stoichiometry of these small particles
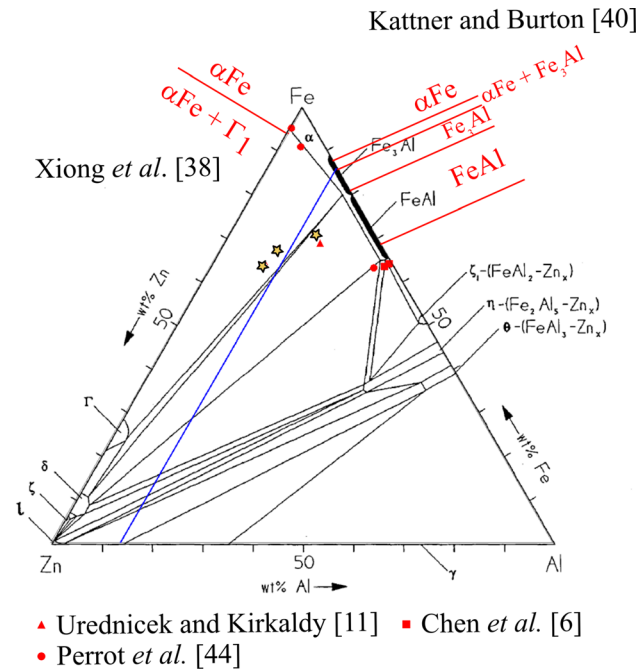
corresponds to Fe$_3$Al (blue line in Figure 7) containing Zn (Fe/Al ~ 2.6 with 22.8 $\pm$ 5.2 mol pct Al, 58.4 $\pm$ 2.7 mol pct Fe, 14.0 $\pm$ 4.2 mol pct Zn, Section III–B–3). Their mean compositions are located outside the αFe region in the ternary diagram used by the galvanizers (yellow stars, Figure 7.[3,4]).

As one would have expected these small particles to be in equilibrium with δ, two questions can be discussed, (i) the mechanism of Fe$_3$Al formation and (ii) the reliability of the Al-Fe-Zn diagram in the Fe-rich corner.

b. Mechanisms of Fe$_3$Al formation The small particles analyzed by APT (Section III–B–3) could be iron particles detached from the steel substrate during the first step of dissolution in liquid zinc. These suspended particles could then be enriched in Al and Zn by solid-state diffusion. The diffusion coefficient of Al in solid iron $D_{Al}^{\alpha Fe}$ at 450 °C is equal to 9.1 $\times$ 10^{-22} m^2/s (extrapolated from measurements performed at temperatures higher than 900 °C[37]). The Al characteristic diffusion time in an αFe spherical particle of radius r = 10 nm, $t_{diff} = \frac{r^2}{D_{Al}^{\alpha Fe}}$, is about 31 hours. As t_{diff} is much higher than the immersion time t_{im} (~ 2 second, Table II) in the galvanizing bath, the proposed mechanism, *i.e.*, solid-state diffusion of Al in Fe particles, can be ruled out.

Another mechanism based on solid-state transformations can be proposed. Fe$_3$Al particles may not be present at 450 °C but may form during cooling of the coating. The solubility of iron in δ decreases by about 2.5 wt pct (based on the Fe-Zn binary diagram[38,39]) when the temperature decreases from 450 °C to room temperature. An order of magnitude of the average number of Fe$_3$Al particles in the tips analyzed by APT can then be estimated. The mass of iron per unit area released by δ during cooling is 3.9 $\times$ 10^{-5} kg/m^2 maximum (given by 0.025 $\cdot \rho_\delta \cdot e_\delta$, where ρ_δ is the δ density and e_δ its thickness with the values given in Section IV–A–2). The mass of iron present in a single particle of Fe$_3$Al assumed spherical is about 2.4 $\times$ 10^{-20} kg, estimated by $\rho_{Fe_3Al} \cdot \frac{\pi}{6} D^3 \cdot w_{Fe}^{Fe_3Al}$, where ρ_{Fe_3Al} is the Fe$_3$Al density (6650 km/m^3, CIF file no. 57793[24,25]), D is the mean particle diameter (about 20 nm, Section III–B–3) and $w_{Fe}^{Fe_3Al}$ is the weight fraction of Fe in Fe$_3$Al (86 wt pct)). Finally, there could be 1.6.10^{15} Fe$_3$Al particles per m^2 in δ and 4 particles on average in each APT tip. Fe$_3$Al particles could therefore be found and analyzed by APT in all tips and thus be formed during cooling. However, this estimate of 4 particles per tip is overestimated by the calculation assumptions. In particular, it is assumed that δ is at thermodynamic equilibrium, even at low temperature, to estimate the iron released by δ during cooling. This leads to an overestimation of the amount of Fe precipitating in Fe$_3$Al. Furthermore, with such a mechanism, the small particles should preferentially be located in the δ region containing the highest amount of Fe, *i.e.*, at the steel/δ or Fe$_2$Al$_5$Zn$_x$/δ interfaces, which is not the case.

Finally, mechanisms involving solid-state reactions may be excluded. The formation of Fe$_3$Al in the liquid metal at the same time as δ is more likely. As told before, the establishment of an iron supersaturation at the steel/liquid zinc interface leads to the nucleation and growth of the inhibition layer. The Fe content in δ is low compared to the Zn content. The Fe supersaturation could therefore be consumed by the formation of α(Fe,Al) particles together with δ, the system studied tending to reach thermodynamic equilibrium between both phases. The Al content is also high in the particles (~ 13 wt pct). Al can come from the liquid Zn bath as for the Fe$_2$Al$_5$Zn$_x$ growth and from the partial dissolution of Fe$_2$Al$_5$Zn$_x$ which is metastable at the liquid zinc bath interface.

In conclusion, if the particles are formed in the liquid phase together with δ rather than by solid-state reactive diffusion, thermodynamic equilibrium between Fe$_3$Al and δ could be achieved, facilitated by the high diffusion rate in liquid state. This led us to study the reliability of the Al-Fe-Zn diagram in the Fe-rich corner.

c. Reliability of the Al-Fe-Zn diagram in the Fe-rich corner A discussion on the construction of the Fe-rich corner of the Al-Fe-Zn diagram is summarized here. In the Fe-rich portion of the Al-Fe binary system, the body-centered cubic (bcc) phases are ordered α'FeAl (B2), ordered α''Fe$_3$Al (D0$_3$), and disordered αFe (A2).[40–42] At 450 °C, the stable phases are αFe, αFe in equilibrium with α''Fe$_3$Al, α''Fe$_3$Al, and α'FeAl when the Al content is increased from 0 to 30 wt pct. For the Fe-Zn binary system, the solubility of Zn in the body-centered cubic (bcc) αFe (A2) is about 5 mol pct (5.8 wt pct) at 450 °C.[38,39,43] The most recent Al-Fe-Zn ternary phase diagram at 450 °C[3,4] was constructed in agreement with the experimental data available in the Fe-rich corner[6,38,40,44] (Figure 7). The first measurement of the Zn solubility in α(Fe,Al) (red triangle in Figure 7)[11] was high compared to the subsequent measurements[6,40] and for this reason rejected by Tang.[3,4]

However, the composition of the small particles (yellow stars, Figure 7) measured in this work is similar to that reported by Ředníček and Kirkaldy.[11] These similar results suggest that the phase diagram currently used in the galvanizing community could be wrong in the Fe-rich corner and that Fe$_3$Al could dissolve much more zinc than reported in Tang's diagram (which relies on very little experimental data in the Fe-rich corner). With such an assumption, the small particles of Fe$_3$Al-containing Zn should then be at thermodynamic equilibrium with δ.

2. ζ rod crystals

Metastable ζ rod crystals have also been observed within the inhibition layer of both steels (Figure 1). Two mechanisms were proposed in the literature to explain their formation: ζ crystals can be formed due to epitaxial relationships with Fe$_2$Al$_5$Zn$_x$ during immersion in the zinc bath[8,9,17,18]; or randomly oriented ζ crystals can

be formed from the Fe supersaturation of the liquid zinc coating during its rapid solidification.[9] Our observations and characterizations do not allow us to decide between these two mechanisms or a new one (such as epitaxial relationships with δ). Understanding the formation mechanisms of ζ requires additional characterizations that were outside the scope of the work presented here.

V. CONCLUSION

In the galvannealing process, the steel strip is immersed in a molten zinc bath containing 0.100 to 0.135 wt pct Al at 450 °C. The coating formed is composed of a thin intermetallic compounds' layer called the inhibition layer (~ 200 nm) covered with a thick zinc layer (~ 10 μm).

The inhibition layer formed on industrial low-alloyed steels was characterized by complementary analysis techniques, in particular transmission electron microscopy and atom probe tomography. Two Al contents in the bath were investigated: 0.112 and 0.128 wt pct.

In both cases, the inhibition layer is composed of a very thin layer of $Fe_2Al_5Zn_x$ and a thicker layer of δ on top of it. The main difference observed in the structure of both inhibition layers is the discontinuity of $Fe_2Al_5Zn_x$ in the case of the lowest bath Al content. The microstructure of the inhibition layer can be described by diffusion paths drawn on the Al-Fe-Zn ternary isothermal section. It means that all interfaces of the inhibition layer are at thermodynamic equilibrium.

The formation of the inhibition layer is proposed to occur with the following reaction mechanisms: Fe dissolution, Fe supersaturation at the steel/liquid Zn interface, and nucleation of metastable $Fe_2Al_5Zn_x$ due to epitaxial relationships with ferrite and nucleation and growth of δ.

Small particles of about 20 nm in size are present in the δ phase and were analyzed to be Fe_3Al-containing Zn. These small particles are proposed to nucleate in the liquid phase at the same time as δ from the Fe supersaturation (coming from the Fe dissolution step). With this mechanism occurring in the liquid state, thermodynamic equilibrium between Fe_3Al and δ could be reached. This led us to question the reliability of the Al-Fe-Zn diagram in the Fe-rich corner (which relies on very little experimental data in the Fe-rich corner).

From an industrial point of view, the results obtained are general for the galvannealing treatment of low-alloyed Interstitial-Free Titanium steels. Research in our group has shown that, in the case of Advanced High Strength Steels, the inhibition layer formed is also composed of a $Fe_2Al_5Zn_x$ layer (which can be continuous or discontinuous depending on the Al content in the galvannealing bath) and a δ layer. In the case of these steels, oxide particles, formed by selective oxidation in the continuous annealing furnace located before the liquid metal bath, are embedded in the inhibition layer.[47] Knowledge of the exact nature of the inhibition layer can lead to robust models to improve the management of industrial galvanizing/galvannealing lines.

The first model could describe the kinetics of reactions occurring in the GA galvanizing bath (as already exists for coatings obtained in liquid zinc containing higher levels of Al[31,32]) and thus help to better control the Al content of liquid zinc. The second model could describe the growth of Fe-Zn phases in the galvannealing furnace located at the exit of the liquid metal bath. This growth begins with the breakdown of the inhibition layer and this breakdown, for example, the time required for breakdown, is highly dependent on the continuity or discontinuity of the $Fe_2Al_5Zn_x$ layer. The first equations of such a model can be found in Reference 48.

ELECTRONIC SUPPLEMENTARY MATERIAL

The online version of this article (https://doi.org/10.1007/s11661-020-05669-5) contains supplementary material, which is available to authorized users.

REFERENCES

1. A.R. Marder: *Prog. Mater. Sci.*, 2000, vol. 45, pp. 191–271.
2. M. Guttmann: *Mater. Sci. Forum*, 1994, vol. 155 (156), pp. 527–48.
3. N.Y. Tang: *Mater. Sci. Technol.*, 1995, vol. 11, pp. 870–73.
4. N.Y. Tang: *J. Phase Equilibria*, 2000, vol. 21, pp. 70–77.
5. J.R. McDermid, M.H. Kaye, and W.T. Thompson: *Metall. Mater. Trans. B.*, 2007, vol. 38B, pp. 215–30.
6. Z.W. Chen, R.M. Sharp, and J.T. Gregory: *Mater. Sci. Technol.*, 1990, vol. 6, pp. 1173–76.
7. Y. Leprêtre, J.M. Mataigne, M. Guttmann, J. Philibert: in *Zinc-Based Steel Coating Systems: Production and Performance*, F.E. Goodwin, eds., The Minerals, Metals & Materials Society, Warrendale, 1998, pp. 95–106.
8. J.M. Mataigne: *Rev. Métall.*, 2009, vol. 106, pp. 27–33.
9. Y. Leprêtre: Ph.D. Thesis, Université Paris XI Orsay, 1996 (in French).
10. L. Chen, R. Fourmentin, and J.R. McDermid: *Metall. Mater. Trans. A*, 2008, vol. 39A, pp. 2128–42.
11. M. Úředníček and J.S. Kirkaldy: *Z. Met. Kd.*, 1973, vol. 64, pp. 899–910.
12. M. Saito, Y. Uchida, T. Kittaka, Y. Hirose, and Y. Hisamatsu: *Tetsu-to-hagané*, 1991, vol. 77, pp. 947–54.
13. M. Sugiyama, M. Okada, and Y. Takada: *J. Jpn. Inst. Met.*, 2001, vol. 65, pp. 397–403 (in Japanese).
14. A.I. Vitkin, G.A. Kokorin, A.G. Grishko, and P.A. Tyukanov: *Met. Sci. Heat Treat.*, 1973, vol. 15, pp. 332–34.
15. H. Yamaguchi and Y. Hisamatsu: *Trans. Iron Steel Inst. Jpn.*, 1979, vol. 19, pp. 649–58.
16. S. Dionne, G. Botton, M. Charest, F. Goodwin: *Proceedings International Symposium on Materials in the Automotive Industry*, E. Essadiqi, F. Goodwin, and M. Elboujdani, eds., Toronto, 2001, pp. 351–65.
17. Y. Adachi, T. Nakamori, and K. Kamei: *J. Jpn. Inst. Met.*, 1992, vol. 56, pp. 1235–41 (in Japanese).

18. E.T. McDevitt and M. Meshii: in *Zinc-Based Steel Coating Systems: Production and Performance*, F.E. Goodwin, ed., The Minerals, Metals & Materials Society, Warrendale, 1998, pp. 127–36.
19. R. Mishra: *Metall. Mater. Trans. A*., 2008, vol. 39A, pp. 2275–77.
20. D. Zapico-Álvarez, F. Bertrand, J.-M. Mataigne, and M.-L. Giorgi: *Metall. Res. Technol*., 2014, vol. 111, pp. 9–15.
21. A.K. Rosiwal: *Verhandlungen der K.K. Geolog*, Reichsanstalt, Wien, 1998, vol. 5, pp. 143–74.
22. N.L. Okamoto, K. Tanaka, A. Yasuhara, and H. Inui: *Acta Crystallogr. B*, 2014, vol. 70, pp. 275–82.
23. P. Stadelmann: JEMS Java Electron Microscopy Simulation Software, http://www.jems-saas.ch/Home/jemsWebSite/jems.html, Oct. 01, 2014, Web. Dec. 25, 2017.
24. G. Bergerhoff and I.D. Brown: in *Crystallographic Databases*, F.H. Allen *et al*., hrsg., International Union of Crystallography, Chester, 1987.
25. A. Belsky, M. Hellenbrandt, V.L. Karen, and P. Luksch: New Developments in the Inorganic Crystal Structure Database (ICSD): Accessibility in Support of Materials Research and Design*Acta Cryst*., 2002, vol. 58, pp. 364–69.
26. U. Burkhardt, Y. Grin, M. Ellner, and K. Peters: *Acta Crystallogr. B*, 1994, vol. 50, pp. 313–16.
27. B. Gault, M.P. Moody, J.M. Cairney, and S. Ringer: *Atom Probe Microsc*, Springer, New York, 2012.
28. H. Benallali, K. Hoummada, M. Descoins, P. Rueda-Fonseca, L. Gerard, E. Bellet-Amalric, S. Tatarenko, K. Kheng, and D. Mangelinck: *Scr. Mater*., 2013, vol. 69, pp. 505–08.
29. J.B. Clark: *Trans. Met. Soc. AIME*, 1963, vol. 227, pp. 1250–51.
30. J.S. Kirkaldy and L.C. Brown: *Can. Metall. Q*., 1963, vol. 2, pp. 89–115.
31. M.L. Giorgi, J.B. Guillot, and R. Nicolle: *J. Mater. Sci*., 2005, vol. 40, pp. 2263–68.
32. M.-L. Giorgi: École Centrale Paris, 2000 (in French).
33. H. Yamaguchi and Y. Hisamatsu: *Tetsu-to-Hagane*, 1973, vol. 59, pp. 131–41.
34. E. McDevitt, Y. Morimoto, and M. Meshii: *ISIJ Int*., 1997, vol. 37, pp. 776–82.
35. K.K. Wang, L. Chang, D. Gan, and H.P. Wang: *Thin Solid Films*, 2010, vol. 518, pp. 1935–42.
36. JW Christian: *The Theory of Transformations in Metals and Alloys—Part 1 Equilibrium and General Kinetic Theory*, 2nd ed., Pergamon Press, Oxford, 1975, pp. 418–28.
37. H. Oikawa: *Trans. Iron Steel Inst. Jpn*., 1982, vol. 68, pp. 1489–97.
38. W. Xiong, Yi Kong, Du Yong, Z.-K. Liu, M. Selleby, W.H. Sun: CALPHAD., 2009, vol. 33, pp. 433–40.
39. H. Okamoto: *Phase Equilib. Diffus*., 2016, vol. 37, pp. 621–34.
40. U.R. Kattner and B.P. Burton: in *Phase Diagrams of Binary Iron Alloys*, H. Okamoto, ed., ASM International, Materials Park, OH, 1993, pp. 12–28.
41. B. Sundman, I. Ohnuma, N. Dupin, U.R. Kattner, and S.G. Fries: *Acta Mater*., 2009, vol. 57, pp. 2896–2908.
42. M.H.G. Jacobs and R. Schmid-Fetzer: *CALPHAD*, 2009, vol. 33, pp. 170–78.
43. B.P. Burton and P. Perrot: in *Phase Diagrams of Binary Iron Alloys*, H. Okamoto, ed., ASM International, Materials Park, OH, 1993, pp. 459–66.
44. P. Perrot, J.-C. Tissier, and J.-Y. Dauphin: *Z. Met. Kd*., 1992, vol. 83, pp. 786–90.
45. L.N. Larikov: *Avt. Svarka*, 1968, vol. 5, pp. 68–69.
46. D. Naio and M. Kajihara: *Mater. Sci. Eng. A*, 2007, vol. 459, pp. 375–82.
47. A. Paunoiu: PhD thesis, Paris-Saclay University, CentraleSupélec, 2018.
48. D. Zapico Álvarez, F. Bertrand, J.-M. Mataigne, and M.-L. Giorgi: *Association for Iron and Steel Technology AIST, Proceedings of Galvatech'2015, 10th International Conference on Zinc and Zinc Alloy Coated Steel Sheet*, Toronto, 2015, pp. 307–15.